Momentum-resolved superconducting energy gaps of Sr_2RuO_4 from quasiparticle interference imaging

Rahul Sharma[a,b], Stephen D. Edkins[c], Zhenyu Wang[d], Andrey Kostin[a,b], Chanchal Sow[e,f], Yoshiteru Maeno[e], Andrew P. Mackenzie[g,h], J. C. Séamus Davis[a,g,i,j,1], and Vidya Madhavan[d,1]

[a]Laboratory of Atomic and Solid State Physics, Department of Physics, Cornell University, Ithaca, NY 14853; [b]Condensed Matter Physics and Material Science Department, Brookhaven National Laboratory, Upton, NY 11973; [c]Department of Applied Physics, Stanford University, Stanford, CA 94305; [d]Department of Physics, University of Illinois, Urbana, IL 61801; [e]Department of Physics, Kyoto University, 606-8502 Kyoto, Japan; [f]Department of Physics, Indian Institute of Technology-Kanpur, 208016 Uttar Pradesh, India; [g]Physics of Quantum Materials Department, Max Planck Institute for Chemical Physics of Solids, D-01187 Dresden, Germany; [h]School of Physics and Astronomy, University of St. Andrews, North Haugh, St. Andrews KY16 9SS, United Kingdom; [i]Clarendon Laboratory, University of Oxford, Oxford OX1 3PU, United Kingdom; and [j]Department of Physics, University College Cork, T12R5C Cork, Ireland

Contributed by J. C. Séamus Davis, January 21, 2020 (sent for review September 23, 2019; reviewed by Milan P. Allan and Ilya Eremin)

Sr_2RuO_4 has long been the focus of intense research interest because of conjectures that it is a correlated topological superconductor. It is the momentum space (*k*-space) structure of the superconducting energy gap $\Delta_i(k)$ on each band *i* that encodes its unknown superconducting order parameter. However, because the energy scales are so low, it has never been possible to directly measure the $\Delta_i(k)$ of Sr_2RuO_4. Here, we implement Bogoliubov quasiparticle interference (BQPI) imaging, a technique capable of high-precision measurement of multiband $\Delta_i(k)$. At $T = 90$ mK, we visualize a set of Bogoliubov scattering interference wavevectors $\mathbf{q}_j : j = 1-5$ consistent with eight gap nodes/minima that are all closely aligned to the $(\pm 1, \pm 1)$ crystal lattice directions on both the α and β bands. Taking these observations in combination with other very recent advances in directional thermal conductivity [E. Hassinger *et al.*, *Phys. Rev. X* 7, 011032 (2017)], temperature-dependent Knight shift [A. Pustogow *et al.*, *Nature* 574, 72–75 (2019)], time-reversal symmetry conservation [S. Kashiwaya *et al.*, *Phys. Rev B*, 100, 094530 (2019)], and theory [A. T. Rømer *et al.*, *Phys. Rev. Lett.* 123, 247001 (2019); H. S. Roising, T. Scaffidi, F. Flicker, G. F. Lange, S. H. Simon, *Phys. Rev. Res.* 1, 033108 (2019); and O. Gingras, R. Nourafkan, A. S. Tremblay, M. Côté, *Phys. Rev. Lett.* 123, 217005 (2019)], the BQPI signature of Sr_2RuO_4 appears most consistent with $\Delta_i(k)$ having $d_{x^2-y^2}$ (B_{1g}) symmetry.

strontium ruthenate | quasiparticle interference | superconducting energy gaps

Determining the structure and symmetry of the superconducting energy gaps $\Delta_i(k)$ for Sr_2RuO_4 has been a longstanding objective (1–4) but one on which radically new perspectives have emerged recently. The linearity with temperature of electronic specific heat capacity at lowest temperatures (5), the temperature dependence of London penetration depth (6), the attenuation rate of ultrasound (7), and field-oriented specific heat measurements (8) have long implied the existence of nodes (or profound minima) somewhere in $\Delta_i(k)$. However, recent thermal conductivity measurements further indicate that these nodes/minima are oriented parallel to the crystal *c* axis (9). Moreover, in-plane ^{17}O NMR reveals a very substantial drop of the Knight shift (10) below T_c. Additionally, no cusp occurs in the superconducting critical temperature under uniaxial strain (11, 12). Finally, current-field inversion experiments using Josephson tunnel junctions indicate that time-reversal symmetry (TRS) is preserved (13). This phenomenology is in sharp contradistinction to the Sr_2RuO_4 ancien regime under which ^{17}O Knight shift (14) and spin-polarized neutron scattering (15) reported no diminution in spin susceptibility below T_c and where muon spin rotation (16) and Kerr effect (17) indicated TRS breaking. Therefore, an extensive reassessment of the theory of Sr_2RuO_4 superconductivity has quickly materialized (18–23).

Although the crystal is isostructural with the *d*-wave high-temperature superconductor La_2CuO_4 (Fig. 1*A*), for Sr_2RuO_4 the Fermi surface (FS) consists of three sheets (24, 25) (Fig. 1*B*). Hybridization between the two quasi-one-dimensional bands that originate from the Ru d_{xz} and d_{yz} orbitals leads to the electron-like β band surrounding the Γ point (red in Fig. 1*B*) and hole-like α band surrounding the X point (blue in Fig. 1*B*); similarly, the Ru d_{xy} orbitals generate the electron-like, quasi-two-dimensional γ band surrounding the Γ point (green in Fig. 1*B*). Correctly representing the electron–electron interactions is then a complex challenge. Onsite and intersite Coulomb interactions are pervasive; Hund's coupling between the Ru *d* orbitals generates orbital-selective phenomena, rendering the γ band significantly more correlated than the α:β bands (26, 27); and spin-orbit coupling plays a significant role throughout (26). Contemporary theories (18–23, 28, 29) consider various combinations of these interactions to achieve their $\Delta_i(k)$ predictions, focusing on the dependence of symmetry of the predominant $\Delta_i(k)$ on the interplay between them. Weak coupling analyses (28, 29) of Hamiltonians parameterized by the ratio $\rho = J/U$ (*U* and *J* are the onsite Coulomb and Hund's interaction energies, respectively) find that the preferred order parameters exhibit E_u(chiral *p* wave) symmetry with $B_{1g}(d_{x^2-y^2})$ symmetry as a subdominant solution (28) and E_u(chiral *p* wave) or A_{1u}(helical *p* wave) symmetry but with $B_{1g}(d_{x^2-y^2})$ symmetry also as a subdominant solution (29). More recent theories parameterized by both $\rho = J/U$ and spin-orbit coupling λ find that the order parameters filling large (but different) portions of the

Significance

Sr_2RuO_4 has been widely studied as a candidate correlated topological superconductor. However, the momentum space structure of the superconducting energy gaps, which encode both the pairing mechanism and its topological nature, has proven impossible to determine by conventional techniques. To address this challenge, we introduce Bogoliubov quasiparticle scattering interference visualization at millikelvin temperatures. We discover that the α and β bands of Sr_2RuO_4 support thermodynamically prevalent superconducting energy gaps and that they each contain four gap nodes (or profound minima) that are contiguous to the $(0,0) \to (\pm 1, \pm 1)\pi/a$ lines in momentum space. In the context of other recent advances, these observations appear most consistent with a $d_{x^2-y^2}$ order parameter symmetry for Sr_2RuO_4.

Author contributions: A.P.M., J.C.S.D., and V.M. designed research; R.S., S.D.E., Z.W., and J.C.S.D. performed research; C.S. and Y.M. contributed new reagents/analytic tools; R.S., S.D.E., Z.W., A.K., and J.C.S.D. analyzed data; and R.S., S.D.E., Z.W., A.P.M., J.C.S.D., and V.M. wrote the paper.

Reviewers: M.P.A., Leiden University; and I.E., Ruhr-Universität Bochum.

The authors declare no competing interest.

Data deposition: The authors can be contacted to provide the raw data.

[1]To whom correspondence may be addressed. Email: jcseamusdavis@gmail.com or vm1@illinois.edu.

This article contains supporting information online at https://www.pnas.org/lookup/suppl/doi:10.1073/pnas.1916463117/-/DCSupplemental.

First published February 24, 2020.

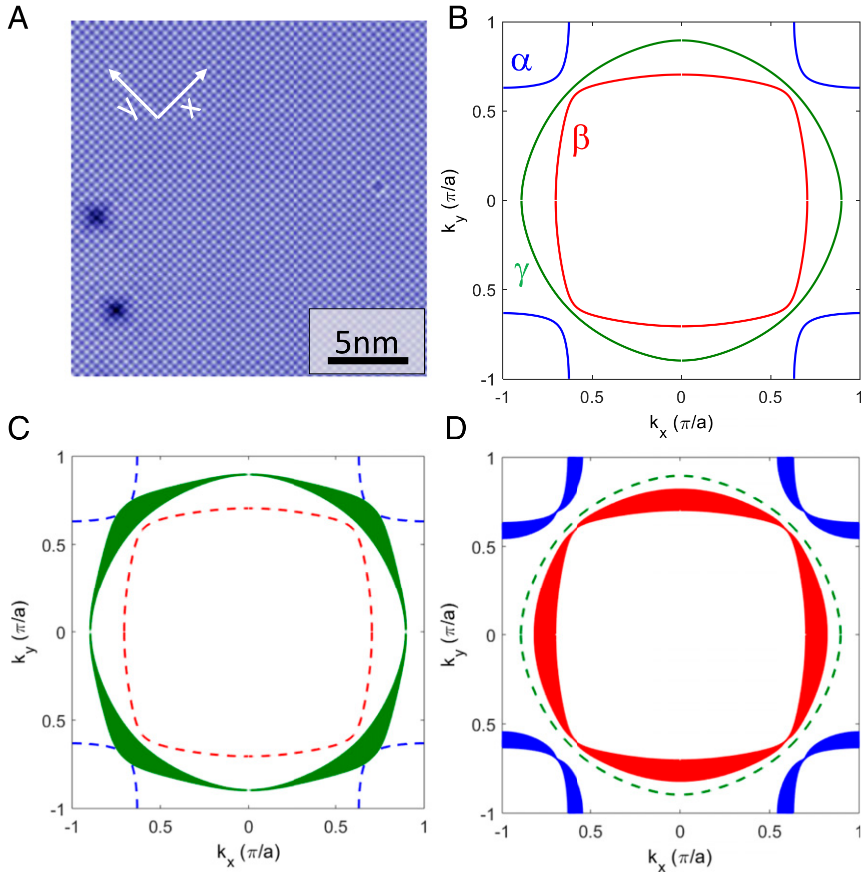

Fig. 1. Electronic structure of superconducting Sr_2RuO_4. (*A*) Topographic image of the surface of Sr_2RuO_4 recorded at V_s = 100 mV and I_s = 100 pA showing SrO plane and defects, which are Sr vacancies. All experiments reported in this paper were carried out under equivalent topographic conditions. (*B*) Model FS of Sr_2RuO_4 showing α (blue), β (red), and γ (green) bands. (*C*) Pedagogical model of a superconducting energy gap on γ band with gap minima along (±1,0); (0, ±1). (*D*) Pedagogical model of superconducting energy gaps on α:β bands with gap minima along (±1, ±1).

ρ−λ-phase space exhibit $B_{1g}(d_{x^2-y^2})$ symmetry (18–20) and A_{1u}(helical *p* wave) symmetry (18, 19) or even more complex spin-triplet orders (20). One surprising consequence is that the field-in-plane Knight shift does not discriminate strongly between $\Delta_i(k)$ having $d_{x^2-y^2}$ (even parity) or $p_{helical}$ (odd parity) order parameters (18, 19). Obviously, what could discriminate between all of these different order parameter symmetries is the fully detailed structure of $\Delta_i(k)$ as shown, for example, in figure 2 of ref. 18 or figure S3 of ref. 19.

However, although critical to testing advanced theories (18–23) for superconductivity in Sr_2RuO_4, the $\boldsymbol{k}$-space structure of $\Delta_\alpha(\boldsymbol{k}); \Delta_\beta(\boldsymbol{k}); \Delta_\gamma(\boldsymbol{k})$ has never been measured directly. Basically, this is because the maximum magnitude of any of these gaps (30, 31) is $|\Delta| \leq 350$ μeV so that temperature $T \lesssim 100$ mK and energy resolution with $\delta E \lesssim 100$ μeV are required to spectroscopically detect strongly anisotropic $\boldsymbol{k}$-space gap structures and/or their gap minima. Thus, techniques capable of band-resolved, high-resolution superconducting $\Delta(\boldsymbol{k})$ determination and specifically, of distinguishing the orientation of any gap minima on different bands are required. Bogoliubov quasiparticle interference (BQPI) imaging (32–38) has been proposed (39–41) to achieve these objectives for Sr_2RuO_4 as it has the proven capability of measuring extremely anisotropic (33–38), multiband (35, 36, 38) superconducting energy gaps with energy resolution (36, 38) $\delta E \lesssim 75$ μeV. Intuitively, this is possible because, when a highly anisotropic Δ_k opens on a given band, Bogoliubov quasiparticles $|\boldsymbol{k}(E)\rangle$ exist in the energy range $\Delta_k^{min} < E < \Delta_k^{max}$. Within this range, interference of impurity-scattered quasiparticles produces characteristic real-space ($\boldsymbol{r}$-space) modulations in the density of electronic states (32, 39–41) $\delta N(\boldsymbol{r}, E)$. The Bogoliubov quasiparticle dispersion $E_i(k)$ then exhibits closed constant energy contours surrounding FS $\boldsymbol{k}$-points where minima in Δ_k occur. These $\boldsymbol{k}$-space locations can be determined because $\delta N(\boldsymbol{r}, E)$ modulations occur at the set of wavevectors $q_j(E)$ connecting them. These $q_j(E)$ are identified from maxima in $\delta N(\boldsymbol{q}, E)$, the power spectral density Fourier transform of $\delta N(\boldsymbol{r}, E)$.

For Sr_2RuO_4, BQPI signatures of different types of gap structures [for example, $\Delta_\alpha(\boldsymbol{k}); \Delta_\beta(\boldsymbol{k})$] may be anticipated by using a pedagogical Hamiltonian $H(k) = \sum_k \psi^\dagger(k)\hat{H}(k)\psi(k)$, where

$$\hat{H}(k) = \begin{pmatrix} \epsilon_\alpha(k) & \Delta_\alpha(k) & 0 & 0 \\ \Delta_\alpha^*(k) & -\epsilon_\alpha(k) & 0 & 0 \\ 0 & 0 & \epsilon_\beta(k) & \Delta_\beta(k) \\ 0 & 0 & \Delta_\beta^*(k) & -\epsilon_\beta(k) \end{pmatrix}, \qquad [1]$$

in the basis $\psi^\dagger(k) = (c^\dagger_{\alpha,\boldsymbol{k},\uparrow}, c_{\alpha,-\boldsymbol{k},\downarrow}, c^\dagger_{\beta,\boldsymbol{k},\uparrow}, c_{\beta,-\boldsymbol{k},\downarrow})$ and $\epsilon_\alpha(k)$, $\epsilon_\beta(k)$ are the band dispersion for the α:β bands (39–41). The unperturbed Green's function is $G^0(k,\epsilon) = [(\epsilon + i\delta)I - \hat{H}(k)]^{-1}$, where I is identity matrix and δ is the energy width broadening parameter. Both interband and intraband scattering could be considered using a *T*-matrix for all scattering processes as

$$T^{-1}(\omega) = \left((V_{intra}I + V_{inter}\sigma_x) \otimes \sigma_z\right)^{-1} - \int \frac{dk}{(2\pi)^2} G^0(k,\omega). \qquad [2]$$

However, interband scattering between the α:β and γ bands has not been the subject of any theoretical analysis for Sr_2RuO_4

(39–41); hence, we do not consider it here. The Fourier transform of $\delta N(\boldsymbol{r},E)$ modulations caused by scattering interference of Bogoliubons can be predicted from Eqs. **1** and **2** as

$$\delta N(\boldsymbol{q},E)=-\frac{1}{\pi}Im\sum_{i=1,3}\left[\frac{\int d\boldsymbol{k}}{(2\pi^2)}G_0(\boldsymbol{k}+\boldsymbol{q},E)T(E)G_0(\boldsymbol{k},E)\right]_{ii} \quad [3]$$

where $[\ldots]_{ij}$ denotes Nambu spinor indices (*SI Appendix*, section I). For example, Fig. 1*C* represents BQPI for an anisotropic energy gap $\Delta_\gamma(\boldsymbol{k})$ on the γ band, while Fig. 1*D* represents a BQPI model with anisotropic energy gaps $\Delta_\alpha(\boldsymbol{k})$; $\Delta_\beta(\boldsymbol{k})$ on the α:β bands. The experimental challenge is to visualize Bogoliubov scattering interference in Sr_2RuO_4 and, through comparison with $\delta N(\boldsymbol{q},E)$ predictions (39–41) to determine $\Delta_i(\boldsymbol{k})$.

To do so, we insert high-quality single crystals of Sr_2RuO_4 (T_c = 1.45 K) into a dilution refrigerator-based spectroscopic imaging scanning tunneling microscope (STM) and cleave them in cryogenic ultrahigh vacuum at $T \lesssim 1.8$ K. This typically reveals an atomically flat SrO cleave surface (Fig. 1*A*), although sometimes, the RuO_2 termination layer occurs (31). At the SrO termination surfaces used throughout these studies (Fig. 1*A*), the tip sample differential tunneling conductance $g(\boldsymbol{r},E)\equiv dI/dV(r,E=eV)$ is imaged to visualize scattering interference-induced modulations $g(\boldsymbol{r},E)\propto\delta N(\boldsymbol{r},E)$. In the normal state, $g(\boldsymbol{r},E)$ measurements in the range $-20\text{ meV}<E<20\text{ meV}$ reveal $g(\boldsymbol{q},E)\propto\delta N(\boldsymbol{q},E)$ (Fig. 2*A*) with predominant scattering wavevectors $\boldsymbol{q}(E)$shown as red and blue arrows in Fig. 2*A*. Quantitative comparison with the known FS $\boldsymbol{k}(E=0)$ wavevectors (25) reveals that these arise from intraband scattering in both the β band and the α band (Fig. 1*B*) (*SI Appendix*, section II). As in previous quasiparticle interference studies of normal-state Sr_2RuO_4, the γ band is virtually undetectable, probably because the d_{xy} character leads to small wavefunction overlap for tunneling into the STM tip (31). In any case, the α:β bands are directly identifiable from their normal-state scattering interference wavevectors throughout all of the BQPI studies reported below.

To measure $\Delta_i(\boldsymbol{k})$, we cool each sample to T = 90 mK (*SI Appendix*, section III) and typically measure $g(\boldsymbol{r},E)\propto\delta N(\boldsymbol{r},E)$ on a 128 × 128 grid in a 20-nm field of view. Typical junction formation parameters for these $g(\boldsymbol{r},E)$ measurements are $I_S=40$ pA, $V_S=1$ mV, and $|E|=0$, 100, 200, 300, 400 μeV spanning the maximum superconducting energy gap (*SI Appendix*, section III). The actual electron temperature is manifestly well below ~100 μeV/3.5 k_B or ~300 mK because these BQPI images are distinct when the tip bias voltage is changed in energy steps of 100 μeV. A representative point spectrum from such a map is shown in Fig. 2*C*, showing the typical (30, 31) energy gap maximum $\Delta_{max}\approx 350$ μeV. Fig. 2*D* shows a typical measured $g(\boldsymbol{q},E=100\text{ μeV})$ deep within this superconducting gap. It is highly distinct from the $g(\boldsymbol{q},E)$ measured near E_F in the normal state (Fig. 2*A*) or at $E \gg 350$ μeV in the superconducting state (Fig. 4E), with many robust distinct $\boldsymbol{q}$-space features. Differences in signal intensity between $g(\boldsymbol{q},E=400\text{ μeV})$ measured in the normal and superconducting states occur due to

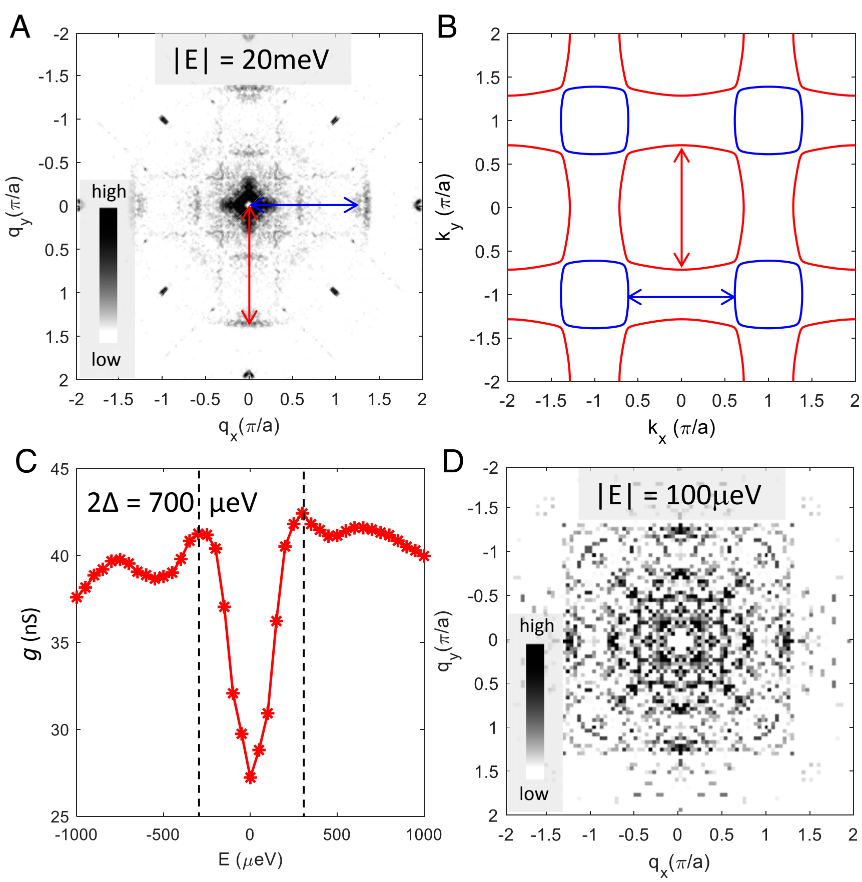

Fig. 2. Visualizing quasiparticle interference from α:β bands and in the superconducting state. (*A*) Measured $g(\boldsymbol{q},E)$ at T = 2.1 K and E = 20 meV in normal state. Arrows show the features resulting from quasiparticle scattering from α (blue) and β (red) bands. (*B*) FS showing α:β bands in red and blue, respectively. Major scattering vectors as detected in experiments are overlaid. (*C*) Spatially averaged superconducting tunneling spectrum showing the full energy gap $\Delta\approx 350$ μeV measured at T = 90 mK. (*D*) Measured $g(\boldsymbol{q},E)$ at T = 90 mK and $E=100$ μeV deep within the superconducting energy gap revealing the highly distinct BQPI pattern of Sr_2RuO_4.

the greatly reduced bias modulation amplitude required for the latter. Most importantly, the distinct $g(\boldsymbol{q},E)$ at $|E| = 0,100,200,300$ μeV at $T = 90$ mK hold the key to understanding the superconducting energy gap structure of Sr_2RuO_4 using Bogoliubov scattering interference (39–41). At the most elementary level, Fig. 2*D* reveals spectroscopically that, consistent with a wide variety of other techniques (5, 7–9), a strong Bogoliubov quasiparticle density of states exists deep within the superconducting gap of this material.

To aid with interpretation of these $g(\boldsymbol{q},E)$ data, we explore a pedagogical model for $\Delta(\boldsymbol{k})$ having gap zeros along $(\pm 1, \pm 1)$ on α:β bands (Fig. 3*A*). In Fig. 3*A*, the hypothetical gap magnitudes $|\Delta_\alpha(\boldsymbol{k})|, |\Delta_\beta(\boldsymbol{k})|$ are indicated by the thickness of the curves overlaid on the α:β FS. Fig. 3*B* identifies the consequent $\boldsymbol{k}$-space regions where, because of minima in $\Delta_\alpha(\boldsymbol{k})$ and $\Delta_\beta(\boldsymbol{k})$, significant quasiparticle density of states is expected as $E \to 0$. The key BQPI wavevectors $q_j; j = 1,2..5$ (Fig. 3*B*) then connect these $\boldsymbol{k}$-space

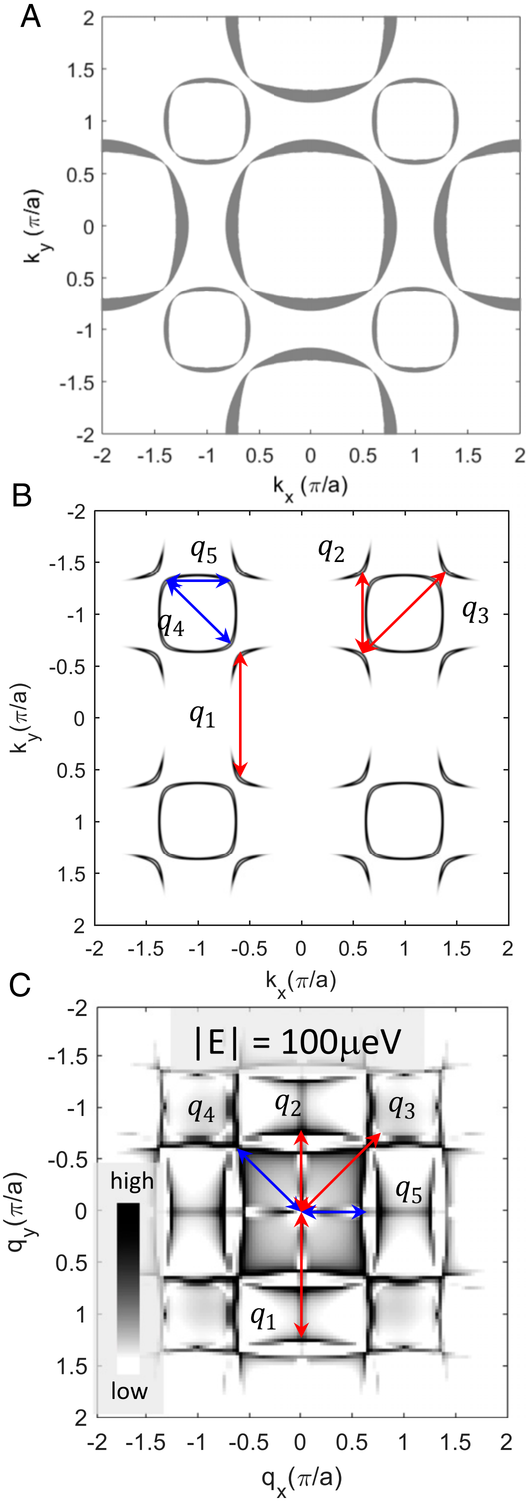

Fig. 3. Pedagogical Bogoliubov scattering interference model. (*A*) Gap magnitude on the FS for α:β band with gap minima along $(\pm 1, \pm 1)$. (*B*) Regions of significant quasiparticle density $E \to 0$ for α:β bands when gapped as shown in *A*. Major scattering vectors are labeled as $q_j; j = 1,2,3,4,5$. (*C*) Calculated $g(\boldsymbol{q},E)$ pattern from Eq. **3** for α:β band from the model in *A* at $E = 100$ μeV. Key scattering wavevectors are indicated by $q_j; j = 1,2,3,4,5$.

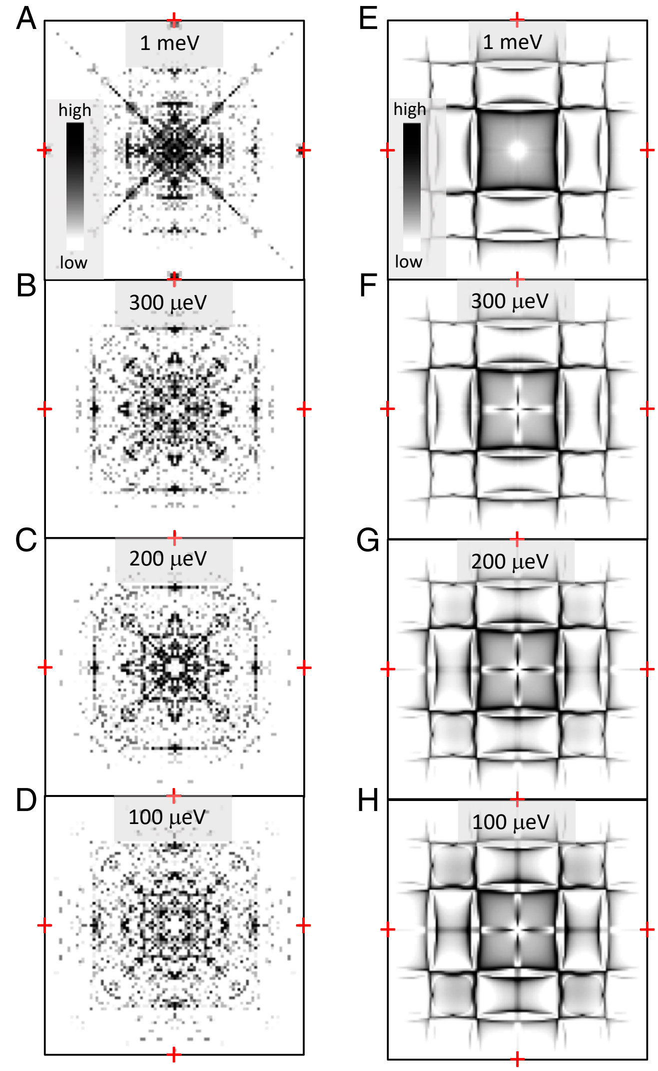

Fig. 4. Imaging Bogoliubov scattering interference of Sr_2RuO_4. (*A–D*) Measured $g(\boldsymbol{q},E)$ images at $T = 90$ mK in superconducting state of Sr_2RuO_4 at $E = 1$ meV, 300 μeV, 200 μeV, and 100 μeV. Red crosses denote Bragg peaks. Typically, the features at lowest $|\boldsymbol{q}|$ in experimental $g(\boldsymbol{q},E)$ represent long-range disorder/drift in the real space rather than any specific low-$|\boldsymbol{q}|$ scattering interference. Moreover, the overall signal intensity here is weak because 1) the density of impurity atoms necessary to avoid suppression of T_c is very low and 2) the low bias voltages and modulations required to visualize BQPI at these extremely low energy scales and with high energy resolution result in greatly increased averaging times per *dI/dV* spectrum. (*E–H*) Predicted $\delta N(\boldsymbol{q},E)$ for α:β bands with minima along $(\pm 1, \pm 1)$ at $E = 1$ meV, 300 μeV, 200 μeV, and 100 μeV. Red crosses denote RuO_2 Bragg peaks.

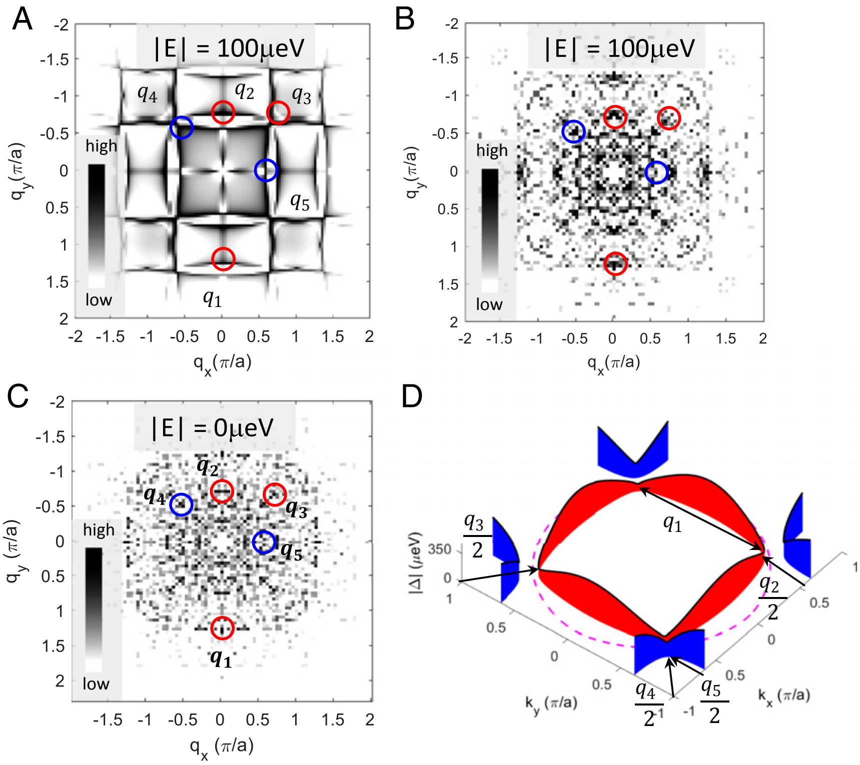

Fig. 5. Predominant $\Delta_\alpha(\boldsymbol{k})$, $\Delta_\beta(\boldsymbol{k})$ with gap minima/nodes along $(\pm1, \pm1)$. (*A*) Predicted $\delta N(\boldsymbol{q}, E)$ for $\Delta_\alpha(\boldsymbol{k})$, $\Delta_\beta(\boldsymbol{k})$ at $E = 100\ \mu$eV with red (blue) circles denoting the features arising from scattering arising from α:β bands. (*B*) Measured $g(\boldsymbol{q}, E)$ pattern at $E = 100\ \mu$eV with circles at similar locations as in *A*. (*C*) Measured $g(\boldsymbol{q}, E)$ pattern at $E = 100\ \mu$eV with circles at similar locations as in *A*. The angular width of maxima at $q_j; j = 3,4$ in this image indicates that minima in $\Delta_\alpha(\boldsymbol{k})$, $\Delta_\beta(\boldsymbol{k})$ occur at less than ~0.05 rad from the $(0,0) \to (\pm1, \pm1)\pi/a$ **k**-space lines. (*D*) Superconducting energy gap $\Delta_i(\boldsymbol{k})$ structure of Sr_2RuO_4 consistent with the $g(\boldsymbol{q}, E)$ data presented here and in Fig. 4.

locations as shown. Fig. 3*C* shows typical evaluations of $\delta N(\boldsymbol{q}, E)$ from Eq. **3** for this model, with the key BQPI wavevectors overlaid. Here q_1, q_2, q_3 (Fig. 3*B*) occur due to the gap minima/nodes on the β band, while q_4, q_5 (Fig. 3*B*) occur due to gap minima/nodes on the α band. Observation of BQPI intensity in $g(\boldsymbol{q}, E)$ data at these specific wavevectors $q_j; j = 1,2..5$ would give direct evidence for a superconducting energy gap structure (Fig. 3*A*) with gap minima/nodes along the $(\pm1, \pm1)$ on the α:β bands of Sr_2RuO_4.

Fig. 4 contains the key experimental results of this study: the measured $g(\boldsymbol{q}, E)$ at multiple energies within the superconducting gap of Sr_2RuO_4 at $T = 90$ mK. The $g(\boldsymbol{q}, E = 1\ \text{meV})$ in Fig. 4*A* is shown for comparison. Predictions from Eq. **3** for $\delta N(\boldsymbol{q}, E)$ with the gap model in Fig. 3*A* are shown at corresponding energies to the measured $g(\boldsymbol{q}, E)$ in Fig. 4 *E–H*. The simultaneously measured $g(\boldsymbol{q}, E = 1\ \text{meV})$ exhibits direct signatures of α:β-band scattering interference as identified from our normal-state studies (*SI Appendix*, section II). Since the electron tunneling manifestly occurs to the α:β bands and simultaneously exhibits a single-particle spectrum showing gap maximum $\Delta_{max} \approx 350\ \mu$eV (Fig. 2*C*), we conclude that this superconducting gap is hosted by the α:β bands (31). Additionally, because $\Delta_{max} \approx 350\ \mu$eV is a consistent gap maximum for the bulk superconducting critical temperature T_c = 1.45 K (because $2\Delta_{max}/kT_c \approx 4$), this indicates that $\Delta_\alpha(\boldsymbol{k}); \Delta_\beta(\boldsymbol{k})$ are principal energy gaps of Sr_2RuO_4.

Then, when Bogoliubov scattering interference is visualized at subgap energies $|E| < \Delta_{max}$, a distinctive $g(\boldsymbol{q}, E)$ pattern emerges. It exhibits clear maxima at specific $\boldsymbol{q}$ vectors (Fig. 4 *B–D*) that evolve but do not disappear as $E \to 0$. Theories of Sr_2RuO_4 BQPI demonstrate how these $\boldsymbol{q}$ vectors encode the direction of the gap minima in $\Delta_\alpha(\boldsymbol{k}); \Delta_\beta(\boldsymbol{k})$ and also predict a very weak dispersion of the subgap $g(\boldsymbol{q}, E)$ with energy (39–41). The observed pattern of $g(\boldsymbol{q}, E = 100\ \mu\text{eV})$ maxima in Fig. 4*D* is quite representative and conforms to predicted $\delta N(\boldsymbol{q}, E = 100\ \mu\text{eV})$ of the energy gap model in Fig. 3. Specifically, in Fig. 5*A*, the predicted BQPI wavevectors q_1, q_2, q_3, q_4, and q_5 from the α:β-band model with nodes/minima along $(\pm1, \pm1)$ (circles in Fig. 5*A*) are compared with the locations of five distinct local maxima in $g(\boldsymbol{q}, E = 100\ \mu\text{eV})$ in Fig. 5*B* and found to be in good agreement. The immediate implication is that eight nodes/minima occur in $\Delta_\alpha(\boldsymbol{k}); \Delta_\beta(\boldsymbol{k})$ at the locations where the α:β bands cross the $(0,0) \to (\pm1, \pm1)\pi/a$ symmetry axes. Because the measured $g(\boldsymbol{q}, E)$ are distinct for $E = 0,100,200,300\ \mu$eV (Fig. 4), the energy resolution δE is demonstrably $\delta E < 100\ \mu$eV, while from the measurement parameters, we estimate that $\delta E \lesssim 75\ \mu$eV. This means that, if minima (as opposed to nodes) occur in $\Delta_\alpha(\boldsymbol{k})$ and $\Delta_\beta(\boldsymbol{k})$, they exist below the energy scale $|E| = 75\ \mu$eV. Moreover, analysis of the $g(\boldsymbol{q}, E = 0)$ data shown in Fig. 5*C* indicates that all eight gap minima/nodes have an angular displacement about (0, 0) in $\boldsymbol{k}$ space within ~±0.05 rad from the $(0,0) \to (\pm1, \pm1)\pi/a$ lines (*SI Appendix*, section IV). No features expected of $\Delta_\gamma(\boldsymbol{k})$(*SI Appendix*, section II) are detected. As to the signature in $g(\boldsymbol{q}, 0)$ of the predicted minima on $\Delta_\beta(\boldsymbol{k})$ in an odd-parity state (figure 2 of ref. 18, figure S3 of ref. 19, and figure 5 of ref. 31), these are expected to appear as $g(\boldsymbol{q}, 0)$ maxima at wavevectors at least ±0.1 rad away from the $(0,0) \to (\pm1, \pm1)\pi/a$ lines (18, 19, 28, 31), or if the energy resolution is insufficient to resolve them, they should exhibit as a broad arc connecting these $g(\boldsymbol{q}, 0)$ maxima. As discussed in *SI Appendix*, section V, neither of these signatures has been detected within the available signal to noise ratio. Moreover, in the same models (18, 19, 28, 31), the minimum that occurs on $\Delta_\alpha(\boldsymbol{k})$ is typically shallow, whereas the measured minimum on $\Delta_\alpha(\boldsymbol{k})$ is deep reaching to within 75 μeV of zero (Fig. 5*C*). Therefore, a gap structure for both $\Delta_\alpha(\boldsymbol{k})$ and $\Delta_\beta(\boldsymbol{k})$ as shown in Fig. 5*D* seems most consistent with our present data.

In this project, we introduced momentum-resolved spectroscopic measurements of the superconducting gap structure in Sr_2RuO_4. They reveal eight nodes or deep minima in $\Delta_\alpha(\boldsymbol{k})$ and $\Delta_\beta(\boldsymbol{k})$, which occur in close proximity to where the $\alpha:\beta$ bands cross the $(0,0) \to (\pm 1, \pm 1)\pi/a$ lines. In light of recent thermal conductivity (9), Knight shift (10), current-field reversal (13) experiments, and advanced theory (18–20, 28, 29), several key implications emerge from this observation. If TRS was actually broken (14–17) by $\Delta_i(\boldsymbol{k})$ of Sr_2RuO_4 but the order parameter has even parity (10), then $s' + id_{x^2-y^2}$ (18) or $d_{xz} + id_{yz}$ (42) states would be plausible. Based on our BQPI data along with thermodynamic/transport studies (6–9), $d_{xz} + id_{yz}$ appears inconsistent because of its circumferential nodes in the $k_x{:}k_y$ plane, but $s' + id_{x^2-y^2}$ (18) might be consistent. However, for such order parameters, the transition temperature should split under a crystal symmetry-breaking field, but that effect is reportedly absent in multiple relevant studies (11, 12, 43–46). On the other hand, if TRS is preserved (13), the BQPI data (Figs. 3 and 4) are most consistent with a helical odd parity $p_{helical}$ order parameter (18, 19, 28) with A_{1u} symmetry or an even parity $d_{x^2-y^2}$ order parameter (18–20, 28) with B_{1g} symmetry. In terms of the detailed $\boldsymbol{k}$-space structure of $\Delta_i(\boldsymbol{k})$, these two cases are distinct. The former exhibits minima but not nodes on the $\alpha{:}\beta$ bands, their $\boldsymbol{k}$-space locations are not constrained by crystal symmetry, and the minima on different bands are not necessarily coaligned in $\boldsymbol{k}$ space (18, 19). The latter exhibits true nodes on both the α and β bands, with $\boldsymbol{k}$-space locations that are constrained precisely by crystal symmetry to lie along the $(\pm 1, \pm 1)$ directions. Our BQPI data (Fig. 4) imply that the four energy gap minima/nodes of both $\Delta_\alpha(\boldsymbol{k})$ and $\Delta_\beta(\boldsymbol{k})$ exist below the energy scale $|E| = 75$ μeV and that they occur within an angular distance from the $(0,0) \to (\pm 1, \pm 1)\pi/a$ $\boldsymbol{k}$-space lines of $\sim\pm 0.05$ rad. Overall, therefore, these observations seem most consistent with a $d_{x^2-y^2}$ order parameter symmetry for Sr_2RuO_4.

Methods

SI Appendix contains descriptions of the simulations of BQPI for Sr_2RuO_4, demonstration of preferential tunneling to the α and β bands, the experimental techniques for imaging BQPI, measurement of the angular distance of gap minima/nodes from $(0,0) \to (\pm 1, \pm 1)$ lines, and the analysis of possible energy gap minima elsewhere in k space. All data used in this study are available upon request from the corresponding author.

ACKNOWLEDGMENTS. We thank B. M. Andersen, P. Coleman, C. Hicks, B. Ramshaw, S. A. Kivelson, S. H. Simon, and A.-M. Tremblay for helpful discussions and communications. R.S. and A.K. acknowledge support from US Department of Energy, Office of Basic Energy Sciences Contract DEAC02-98CH10886. S.D.E. and J.C.S.D acknowledge support from Gordon and Betty Moore Foundation Emergent Phenomena in Quantum Systems Initiative Grant GBMF4544. Y.M. acknowledges support from Japan Society for the Promotion of Science (JSPS) and Grants-in-aid for scientific research (KAKENHI) Grants JP15H05851 and JP15K21717 and from the JSPS Core-to-Core Program. J.C.S.D. acknowledges support from Science Foundation Ireland Award SFI 17/RP/5445 and from European Research Council Award DLV-788932. V.M. acknowledges funding from US Department of Energy, Office of Basic Energy Sciences Award DE-SC0014335.

1. A. P. Mackenzie, Y. Maeno, The superconductivity of Sr_2RuO_4 and the physics of spin-triplet pairing. *Rev. Mod. Phys.* **75**, 657–712 (2003).
2. Y. Maeno, S. Kittaka, T. Nomura, S. Yonezawa, K. Ishida, Evaluation of spin-triplet superconductivity in Sr_2RuO_4. *J. Phys. Soc. Jpn.* **81**, 011009 (2012).
3. C. Kallin, J. Berlinsky, Chiral superconductors. *Rep. Prog. Phys.* **79**, 054502 (2016).
4. A. P. Mackenzie, T. Scaffidi, C.W. Hicks, Y. Maeno, Even odder after twenty-three years: The superconducting order parameter puzzle of Sr_2RuO_4. *npj Qunatum Mater.* **2**, 40 (2017)
5. S. Nishizaki, Y. Maeno, Z. Mao, Changes in the superconducting state of Sr_2RuO_4 under magnetic fields probed by specific heat. *J. Phys. Soc. Jpn.* **69**, 572–578 (2000).
6. I. Bonalde *et al*., Temperature dependence of the penetration depth in Sr_2RuO_4: Evidence for nodes in the gap function. *Phys. Rev. Lett.* **85**, 4775–4778 (2000).
7. C. Lupien *et al*., Ultrasound attenuation in Sr_2RuO_4: An angle-resolved study of the superconducting gap function. *Phys. Rev. Lett.* **86**, 5986–5989 (2001).
8. K. Deguchi, Z. Q. Mao, H. Yaguchi, Y. Maeno, Gap structure of the spin-triplet superconductor Sr_2RuO_4 determined from the field-orientation dependence of the specific heat. *Phys. Rev. Lett.* **92**, 047002 (2004).
9. E. Hassinger *et al*., Vertical line nodes in the superconducting gap structure of Sr_2RuO_4. *Phys. Rev. X* **7**, 011032 (2017).
10. A. Pustogow *et al*., Pronounced drop of ^{17}O NMR Knight shift in superconducting state of Sr_2RuO_4. *Nature* **574**, 72–75 (2019).
11. C. W. Hicks *et al*., Strong increase of T_c of Sr_2RuO_4 under both tensile and compressive strain. *Science* **344**, 283–285 (2014).
12. A. Steppke *et al*., Strong peak in T_c of Sr_2RuO_4 under uniaxial pressure. *Science* **355**, 148 (2017).
13. S. Kashiwaya *et al*., Time-reversal invariant superconductivity of Sr_2RuO_4 revealed by Josephson effects. *Phys. Rev. B* **100**, 094530 (2019).
14. K. Ishida *et al*., Spin-triplet superconductivity in Sr_2RuO_4 identified by ^{17}O Knight shift. *Nature* **396**, 658 (1998).
15. J. A. Duffy *et al*., Polarized-neutron scattering study of the cooper-pair moment in Sr_2RuO_4. *Phys. Rev. Lett.* **85**, 5412–5415 (2000).
16. G. M. Luke *et al*., Time-reversal symmetry-breaking superconductivity in Sr_2RuO_4. *Nature* **394**, 558–561 (1998).
17. J. Xia, Y. Maeno, P. T. Beyersdorf, M. M. Fejer, A. Kapitulnik, High resolution polar Kerr effect measurements of Sr_2RuO_4: Evidence for broken time-reversal symmetry in the superconducting state. *Phys. Rev. Lett.* **97**, 167002 (2006).
18. A. T. Rømer, D. D. Scherer, I. M. Eremin, P. J. Hirschfeld, B. M. Andersen, Knight shift and leading superconducting instability from spin fluctuations in Sr_2RuO_4. *Phys. Rev. Lett.* **123**, 247001 (2019).
19. H. S. Roising, T. Scaffidi, F. Flicker, G. F. Lange, S. H. Simon, Superconducting order of Sr_2RuO_4 from a three-dimensional microscopic model. *Phys. Rev. Research* **1**, 033108 (2019).
20. O. Gingras, R. Nourafkan, A. S. Tremblay, M. Côté, Superconducting symmetries of Sr_2RuO_4 from first-principles electronic structure. *Phys. Rev. Lett.* **123**, 217005 (2019).
21. S. Acharya *et al*., Evening out the spin and charge parity to increase Tc in Sr_2RuO_4. *Commun. Phys.* **2**, 163 (2019).
22. H. G. Suh *et al*., Stabilizing even-parity chiral superconductivity in Sr_2RuO_4. arXiv: 1912.09525v1 (19 December 2019).
23. Z. Wang, X. Wang, C. Kallin, Spin-orbit coupling and spin-triplet pairing symmetry in Sr_2RuO_4. arXiv:1911.01446 (4 November 2019).
24. A. P. Mackenzie *et al*., Quantum oscillations in the layered perovskite superconductor Sr_2RuO_4. *Phys. Rev. Lett.* **76**, 3786–3789 (1996).
25. A. Damascelli *et al*., Fermi surface, surface states, and surface reconstruction in Sr_2RuO_4. *Phys. Rev. Lett.* **85**, 5194–5197 (2000).
26. M. W. Haverkort, I. S. Elfimov, L. H. Tjeng, G. A. Sawatzky, A. Damascelli, Strong spin-orbit coupling effects on the Fermi surface of Sr_2RuO_4 and Sr_2RhO_4. *Phys. Rev. Lett.* **101**, 026406 (2008).
27. M. Kim, J. Mravlje, M. Ferrero, O. Parcollet, A. Georges, Spin-orbit coupling and electronic correlations in Sr_2RuO_4. *Phys. Rev. Lett.* **120**, 126401 (2018).
28. S. Raghu, A. Kapitulnik, S. A. Kivelson, Hidden quasi-one-dimensional superconductivity in Sr_2RuO_4. *Phys. Rev. Lett.* **105**, 136401 (2010).
29. T. Scaffidi, J. C. Romers, and S. H. Simon, Pairing symmetry and dominant band in Sr_2RuO_4. *Phys. Rev. B* **89**, 220510 (2014)
30. M. D. Upward *et al*., Direct observation of the superconducting gap of Sr_2RuO_4. *Phys. Rev. B Condens. Matter Mater. Phys.* **65**, 220512 (2002).
31. I. A. Firmo *et al*., Evidence from tunneling spectroscopy for a quasi-one-dimensional origin of superconductivity in Sr_2RuO_4. *Phys. Rev. B Condens. Matter Mater. Phys.* **88**, 134521 (2013).
32. Q.-H. Wang, D.-H. Lee, Quasiparticle scattering interference in high-temperature superconductors. *Phys. Rev. B Condens. Matter Mater. Phys.* **67**, 020511 (2003).
33. J. E. Hoffman *et al*., Imaging quasiparticle interference in $Bi_2Sr_2CaCu_2O_{8+\delta}$. *Science* **297**, 1148–1151 (2002).
34. T. Hanaguri *et al*., Quasiparticle interference and superconducting gap in $Ca_{2-x}Na_xCuO_2Cl_2$. *Nat. Phys.* **3**, 865–871 (2007).
35. M. P. Allan *et al*., Anisotropic energy gaps of iron-based superconductivity from intraband quasiparticle interference in LiFeAs. *Science* **336**, 563–567 (2012).
36. M. P. Allan *et al*., Imaging Cooper pairing of heavy fermions in $CeCoIn_5$. *Nat. Phys.* **9**, 468–473 (2013).
37. K. Fujita *et al*., Simultaneous transitions in cuprate momentum-space topology and electronic symmetry breaking. *Science* **344**, 612–616 (2014).
38. P. O. Sprau *et al*., Discovery of orbital-selective Cooper pairing in FeSe. *Science* **357**, 75–80 (2017).
39. Y. Gao *et al*., Probing active/passive bands by quasiparticle interference in Sr_2RuO_4. *Phys. Rev. B Condens. Matter Mater. Phys.* **88**, 094514 (2013).
40. A. Akbari, P. Thalmeier, Multiorbital and hybridization effects in the quasiparticle interference of the triplet superconductor Sr_2RuO_4. *Phys. Rev. B Condens. Matter Mater. Phys.* **88**, 134519 (2013).
41. P. Thalmeier, A. Akbari, Quasiparticle scattering image in hidden order phases and chiral superconductors. *J. Magn. Magn. Mater.* **400**, 23–26 (2016).
42. I. Zutić, I. Mazin, Phase-sensitive tests of the pairing state symmetry in Sr_2RuO_4. *Phys. Rev. Lett.* **95**, 217004 (2005).
43. H. Taniguchi *et al*., Higher-Tc superconducting phase in Sr_2RuO_4 induced by in- plane uniaxial pressure. *J. Phys. Soc. Jpn.* **84**, 014707 (2015).
44. H. Yaghuchi, T. Akima, Z. Mao, Y. Maeno, T. Ishiguro, Detailed study of the ac susceptibility of Sr_2RuO_4 in oriented magnetic fields. *Phys. Rev. B Condens. Matter Mater. Phys.* **66**, 214514 (2002).
45. Z. Q. Mao, Y. Maeno, S. NishiZaki, T. Akima, T. Ishiguro, In-plane anisotropy of upper critical field in Sr_2RuO_4. *Phys. Rev. Lett.* **84**, 991–994 (2000).
46. Y.S. Li *et al*., High precision heat capacity measurements on Sr_2RuO_4 under uniaxial pressure. arXiv:1906.07597 (18 June 2019).